ADVANCED ELECTRONIC MATERIALS
Open Access
www.advelectronicmat.de

Magnetosensory Power Devices Based on AlGaN/GaN Heterojunctions for Interactive Electronics

Xingyu Zhou, Qilin Hua, Wei Sha, Jiyuan Zhu, Ting Liu, Chunyan Jiang, Qi Guo, Liang Jing, Chunhua Du, Junyi Zhai, Weiguo Hu,* and Zhong Lin Wang**

The advances in biological magnetoreception and microelectronics have promoted the vigorous development of interactive electronic devices capable of noncontact interaction and control via magnetic fields. Here, a magnetosensory power device (MPD) that integrates a magnetic film ($(\mathrm{(Fe_{90}Co_{10})_{78}Si_{12}B_{10}})$) unit into a cantilever-structured AlGaN/GaN-based high-electron-mobility-transistor is presented. The MPD is capable to not only sense external magnetic field, but also control device output power with the emulation of magnetoreception. Specifically, the device can achieve significant control of output power density (18.04 to 18.94 W mm^{-2}) quasi-linearly with magnetic field stimuli (0–400 mT) at a gate bias of –5 V. In addition, the maximum output power density of the MPD can reach 85.8 W mm^{-2} when a gate bias of 1 V is applied. The simulation and experimental results show that MPD has excellent orientation and magnetic field sensing functions under 0–400 mT magnetic fields. With the intelligent capabilities of magnetic sense and output power control, such interactive electronic devices will have broad application prospects in the fields of artificial intelligence, advanced robotics, and human-machine interfaces.

1. Introduction

Biological studies have suggested that a variety of animals have the ability to perceive the geomagnetic field, including insects,[1] amphibians,[2] reptiles,[3] fish,[4] and birds.[5] Migratory birds, for instance, have been suggested to not only orient themselves by sensing the inclination of the field,[6] but also may deduce their location by discerning minute local variations in the geomagnetic field.[7,8] Driven by the ongoing rapid advance of artificial intelligence (AI), neuroscience, and bionics, the development of bionic smart devices has made significant progress, such as the bionic eye,[9] artificial synapse network,[10] bionic artificial nerve,[11] bionic skins,[12] etc. The biomimetic applications of magnetoreception in nature would be an appealing source from which inspiration can be drawn to develop magnetosensory

---

X. Zhou, Q. Hua, W. Sha, C. Jiang, Q. Guo, L. Jing, J. Zhai, W. Hu, Z. L. Wang
CAS Center for Excellence in Nanoscience
Beijing Key Laboratory of Micro-nano Energy and Sensor
Beijing Institute of Nanoenergy and Nanosystems
Chinese Academy of Sciences
Beijing 101400, China
E-mail: jyzhai@binn.cas.cn; huweiguo@binn.cas.cn; zhong.wang@mse.gatech.edu

X. Zhou, Q. Hua, W. Sha, C. Jiang, Q. Guo, L. Jing, J. Zhai, W. Hu, Z. L. Wang
School of Nanoscience and Technology
University of Chinese Academy of Sciences
Beijing 100049, China

J. Zhu
State Key Laboratory of ASIC and System
School of Microelectronics
Fudan University
Shanghai 200433, China

T. Liu
College of Mathematics and Physics
Beijing University of Chemical Technology
Beijing 100029, China

C. Du
Key Laboratory for Renewable Energy
Beijing Key Laboratory for New Energy Materials and Devices
Beijing National Laboratory for Condensed Matter Physics
Institute of Physics
Chinese Academy of Science
Beijing 100190, China

J. Zhai, W. Hu, Z. L. Wang
Research Center for Optoelectronic Materials and Devices
School of Physical Science and Technology
Guangxi University
Nanning 530004, China

Z. L. Wang
School of Materials Science and Engineering
Georgia Institute of Technology
Atlanta, GA 30332-0245, USA

The ORCID identification number(s) for the author(s) of this article can be found under https://doi.org/10.1002/aelm.202200941.

DOI: 10.1002/aelm.202200941

power devices for interactive electronics.[13,14] Traditional magnetic sensors have been proposed as a way to interact with objects in a touchless manner and move beyond conventional tactile interactions. Such sensors have been applied to magnetosensitive e-skins[15] and wearable magnetic sensors.[16] However, due to their discrete design and low output power density, these magnetic sensors can usually only be used as sensing devices, and therefore require bulky analog amplifiers as actuators, which are difficult to be applied as interactive electronic systems with high integration and high power density. It is encouraging that more and more research is started on magnetic field sensors with flexible electronics. By integrating amplifying circuits, differential circuits, and sensing modules on a flexible material, a freely stretchable magnetosensory electronic system with extremely high sensitivity and signal-to-noise ratio has been successfully developed.[17,18] Different from the giant magnetoresistive (GMR) sensing element and indium–gallium–zinc–oxide (IGZO) thin-film transistors (TFTs) used in the above works, this work realizes a magnetic sensing system on a single electronic component by using the wide-bandgap semiconductor material GaN. On the one hand, compared to traditional Si materials, GaN materials have unique piezoelectric properties. We utilize this mechanism to realize the function of magnetic sensing. On the other hand, based on the wide bandgap characteristic of GaN material which is much higher than that of Si, we simultaneously realize the function of power amplification of multilevel modulation. Therefore, with GaN material, we have successfully developed an integrated system of magnetic sensing and actuation on a single electronic component. The demand for operating power of new intelligent bionic devices has promoted the cross-study of magnetosensory power devices, thereby realizing the integrated interactive electronic system of noncontact sensing and execution.

As the important representative of the power semiconductor materials, III-nitride compound semiconductor materials (GaN, AlN, AlGaN, etc) have important application prospects in the fields of power electronics,[19] due to the high carrier density, high electron mobility, and wide bandgap. More significantly, III-nitrides show obvious spontaneous and piezoelectric polarization, which accounts well for the modulation of the energy band profile and two-dimensional electron gas (2DEG) concentration in the heterojunction.[20–22] Based on coupling effects of semiconductor characteristics and piezoelectric characteristics, the piezotronic effect can be observed in III-nitrides,[23–25] and it opens a window to strain-regulated nanowires,[26,27] LEDs,[28–30] and HEMTs,[31–33] especially in the artificial intelligence devices.[34,35]

Here, we present a bioinspired magnetosensory power device (MPD) that can demonstrate large output power control with the emulation of magnetoreception in nature. The MPD is based on a cantilever-structured AlGaN/AlN/GaN HEMT device integrated with a high magnetic film $(Fe_{90}Co_{10})_{78}Si_{12}B_{10}$. The cantilever structure of the MPD is an ingenious design that can help to amplify the sensitivity of the output current/power in response to the change of external magnetic field. It is observed that MPD has a sensitive magnetic field-power modulation response. Meanwhile, the gate voltage of the MPD can finally control the operating point of the output power, indicating the robust and programmable characteristics of the MPD. According to the experiment and simulation results, the modulation relationship between the output power of the MPD and the external magnetic field is quasi-linear, showing excellent output power control characteristics with magnetic field. This work not only provides insights into the GaN-based magnetosensory power devices, but also promotes the development of high-power interactive electronic and AI smart devices. It can be expected that MPD will have excellent application prospects in interactive electronics, artificial intelligence, and robotics.

2. Results

2.1. The Design and Performance of MPD

The magnetoreception in nature has fascinated scientists due to its unique biological and bionic characteristics. For example, pigeons can locate themselves and determine directions by sensing the geomagnetic field. **Figure 1** illustrates the magnetoreception in birds and bioinspired magnetosensory power device (MPD). The output current and power of the MPD can be modulated by an external magnetic field. The schematic diagram of the birds' navigation and orientation through the geomagnetic field is displayed in Figure 1a. The ability of birds to navigate and orientate is based on the magnetic field-sensing neurons inside the brain, because the current between its synapses can be adjusted by the magnitude and direction of the geomagnetic field.[36] Figure 1b shows the schematic diagram of the cantilever-based MPD. The designed MPD is based on the cantilever-structured AlGaN/GaN high-electron-mobility transistor (HEMT), in which a magnetic thin film ($(Fe_{90}Co_{10})_{78}Si_{12}B_{10}$) is deposited on the front end of the cantilever.[37–40] The enlarged part is the schematic cross-section of the AlGaN/GaN HEMT, where from top to bottom are AlGaN, AlN, GaN, and Si substrates. The thicknesses of AlGaN, AlN, and GaN layers are 30 nm, 1 nm, and 4.3 µm, respectively, and the active region of MPD is 34×34 µm^2, as shown in Supplementary Table S1. When the MPD senses an external magnetic field, the magnetic force on the magnetic film at the front end of the cantilever will cause bending strain on the active region of the MPD. Based on the piezotronic effect, the bending strain of the active region will induce piezoelectric polarization charges in the AlGaN, AlN, and GaN layers, thereby adjusting the AlGaN/AlN/GaN heterojunction energy band and 2DEG concentration, and finally modulating the output current and power of MPD. Therefore, the MPD manifests effective power modulation characteristics under the stimulation of an external magnetic field, realizing high-power interactive electronics with noncontact sensing and control.

The fabrication process of MPD is shown in **Figure 2**a. We first prepare the HEMT device on the AlGaN/AlN/GaN epitaxial wafer, then deposit a magnetic film $(Fe_{90}Co_{10})_{78}Si_{12}B_{10}$ in the front end of the active region, and finally released the cantilever structure of GaN. To fabricate the GaN-based cantilever, we perform a fully dry etching process by using inductively coupled plasma etching (ICP). We first remove GaN layer by anisotropic etching of GaN, and the cantilever structure is laterally released by isotropic etching of Si. The dry etching process has its own

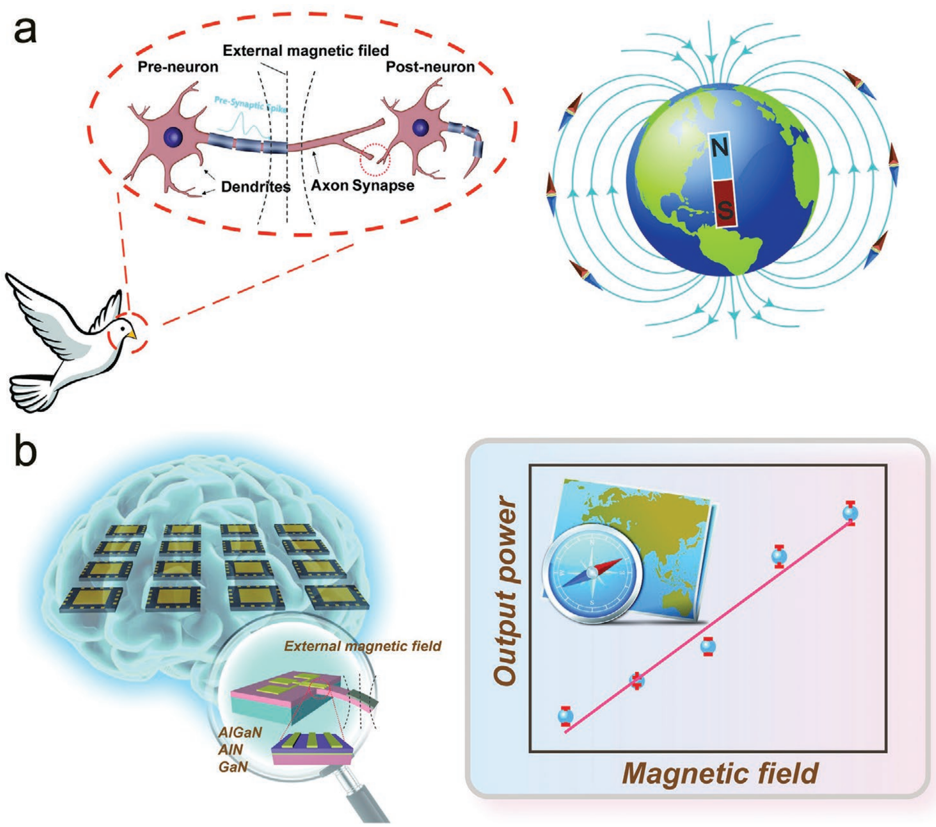

Figure 1. Illustration of the magnetosensory power device (MPD) inspired by magnetoreception in birds. a) Schematic diagram of the birds' navigation and orientation through the geomagnetic field. The current between its synapses inside the brain can be adjusted by the magnitude and direction of the geomagnetic field. b) Schematic diagram of the MPD. The output current and power of the MPD can be significantly modulated by an external magnetic field.

unique advantages, such as precise controllability, patterning, and good repeatability. By simply adjusting the etching time and recipe, we can manufacture the cantilever-based structure MPD under precise control, which is of great significance for the integrated microelectromechanical systems application of MPD. The device fabrication process is also detailed in the Methods. The scanning electron microscope (SEM) image and the inset optical picture taken by CCD camera of Figure 2c clearly displays the manufactured MPD, from which the complete cantilever structure and the HEMT device can be easily observed. The active region is located at the junction between the end of the cantilever and the substrate, and therefore bears the greatest bending strain under the action of external stress, which induces piezoelectric polarization charges in the AlGaN/AlN/GaN interface and modulates the output power of the MPD. The high-resolution TEM image acquired from the AlGaN/AlN/GaN hetero-stacks is displayed in Figure 2c. It is clearly shown that the interface atoms of AlGaN/AlN and AlN/GaN are uniform and sharp without apparent boundary defects or dislocations, and the layers of GaN, AlN, and AlGaN can be easily identified.

The Raman spectroscopy tests on both HEMT and MPD at room temperature have been performed to reveal the influence of the ICP dry etching process on the electrical performance of MPD, as shown in Figure 2e. The MPD exhibits that the E_{2h} phonon mode of GaN shows a blue shift from 568.31 cm^{-1} to 569.33 cm^{-1} compared with the HEMT, which reveals that the dry etching process releases the silicon substrate and relaxes the tensile strain of the GaN layer.[33,41] The alleviation of the tensile strain of the GaN layer will partially weaken the piezoelectric polarization effect of the GaN layer, thereby reducing the 2DEG concentration in the AlGaN/AlN/GaN heterojunction. The relationship between the biaxial stress and the shift of the Raman phonon frequency is shown in Equation (1).

$$\sigma_a = \frac{\Delta\omega}{K_{RS}^{E2(high)}} \tag{1}$$

Where σ_a is the in-plane biaxial stress, $\Delta\omega$ is the shift of the Raman phonon frequency, $K_{RS}^{E2(high)}$ is the Raman biaxial stress conversion factor. We can obtain that the tensile stress of the GaN epitaxial layer is reduced by 352 Mpa compared with that on the Si substrate.[42] In addition, lattice defects have also been introduced during the dry etching process, which reduces the electrical performance of MPD to a certain extent.[43–45] In summary, ICP dry etching will inevitably degrade the performance of the MPD device during the process of preparing the cantilever.

The electrical characteristics of HEMT (before the dry-etching for the cantilever structure) and manufactured MPD are shown in **Figure 3**. Based on the good electrical contact

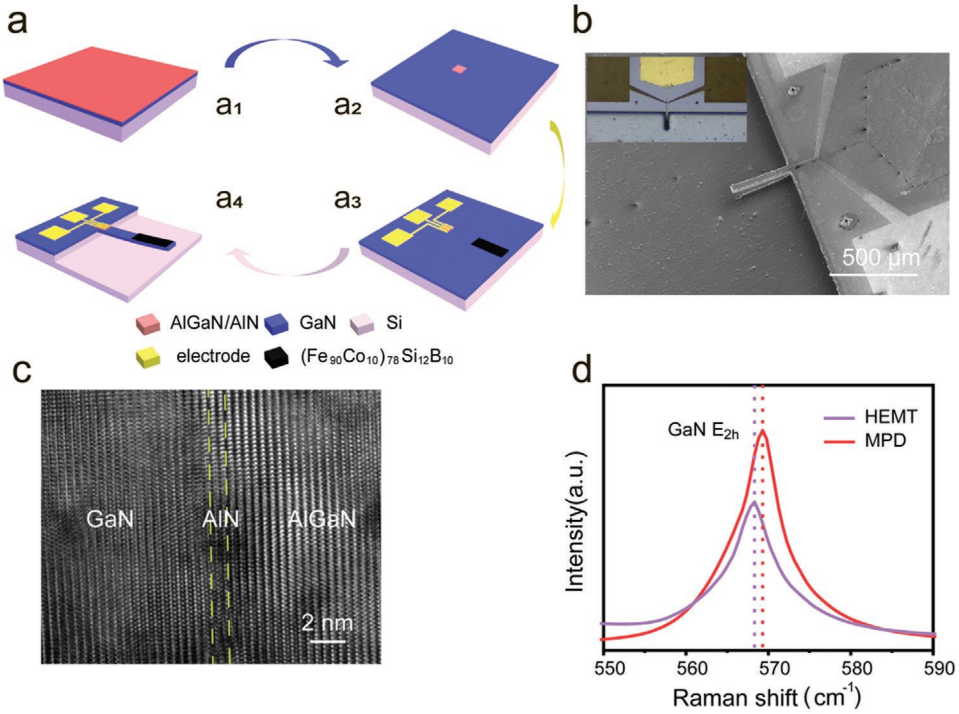

Figure 2. The fabrication process and characterization of MPD. a) The fabrication process flow chart of the MPD. (a1) Initial Si-based AlGaN/AlN/GaN epitaxial layer. (a2) The ≈300 nm of AlGaN, AlN, and GaN mesa isolation etching by $BCl_3/Cl_2/Ar$-based ICP. (a3) Electron beam deposition of Ti (20 nm)/Al (100 nm)/Ni (45 nm)/Au (55 nm) metal stack and Ni (80 nm)/Au (50 nm) metal stacks to prepare Ohmic contact and Schottky contact electrodes, as well as magnetron sputtering deposition of $(Fe_{90}Co_{10})_{78}Si_{12}B_{10}$ (500 nm) magnetic film. (a4) The cantilever is released by ICP-based anisotropic etching of GaN and isotropic etching of silicon, and the size of the cantilever manufactured is $350 \times 60 \times 5\ \mu m^3$. b) Scanning electron microscopy (SEM) image of the MPD, and the inset shows an optical picture taken by CCD camera. c) The high-resolution TEM image acquired from the AlGaN/AlN/GaN hetero-stacks. d) The micro-Raman spectra of the AlGaN/AlN/GaN heterostructures before (HEMT) and after (MPD) dry-etching for the cantilever structure.

performance, the output characteristics ($I_{ds} - V_{ds}$) of both HEMT and MPD have excellent gate control capabilities, as shown in Figure 3a,c, respectively. It is clearly shown that the output current shows good linearity at low source-drain bias (V_{ds}) voltage, and then as the bias voltage further increases, the output current reaches saturation. Both HEMT and MPD can achieve stable large output current above 200 mA mm^{-1} in the saturation region, and can be effectively controlled at various gate voltage V_{gs} from −7 V to 1 V. Compared with HEMT, the saturated output current of MPD under the source-drain bias voltage of 10 V drops from 264 mA mm^{-1} to 197 mA mm^{-1}. Furthermore, we measure the transfer ($I_{ds} - V_{gs}$) characteristics of the HEMT and the MPD at $V_{ds} = 10$ V, as shown in Figure 3b,d, respectively. The maximum transconductance ($g_{m,\max}$) of HEMT is 42.4 mS mm^{-1} (Figure 3c), while the value for the MPD reduces to 32.9 mS mm^{-1} (Figure 3d). The transconductance performance of MPD is also slightly lower than HEMT. The reduction in the output current and transconductance of the MPD can be attributed to the dry etching process, which inevitably leads to stress release and lattice defects in the GaN layer.

Different magnetic fields are applied to the MPD under various gate voltages to mimic the magnetoreception. The modulation characteristics of the external magnetic field on the output current and power of the MPD are systematically discussed. We design a solenoid to apply different magnetic fields to the MPD and place the MPD into the solenoid in the direction perpendicular to the magnetic field line. According to Biot–Savart law, the magnetic field inside the solenoid can be regarded as a uniform magnetic field. By changing the current of the energized solenoid and calibrating with a magnetic field detector, the magnetic field acting on the MPD can be accurately controlled. In this article, we adopt the B-field as the description of the magnetic field, whose unit is T. **Figure 4**a illustrates the strain distribution of the MPD under an external magnetic field of 400 mT, which is simulated by COMSOL Multiphysics and the magnetic force bends the cantilever down perpendicular to the device surface (the device surface is defined as the plane of the active area of the device). It clearly shows that due to the design of the cantilever structure, the active region of the MPD bears the strain under the action of the magnetic field, thereby enhancing the piezotronic effect and increasing the modulation of the output power by the magnetic field. Figure 4b displays the output characteristics of the MPD under an external magnetic field of 200 mT, with the gate voltage V_{gs} ranging from −5 V to 1 V at a step of 1 V. Under the same magnetic field, the modulation effect of the current density becomes more significant with the increase of V_{gs}, which means that the output current response to the external magnetic field is effectively modulated by the gate voltage V_{gs}.

In addition, the output current of the MPD can also be effectively modulated by an external magnetic field. Figure 4c

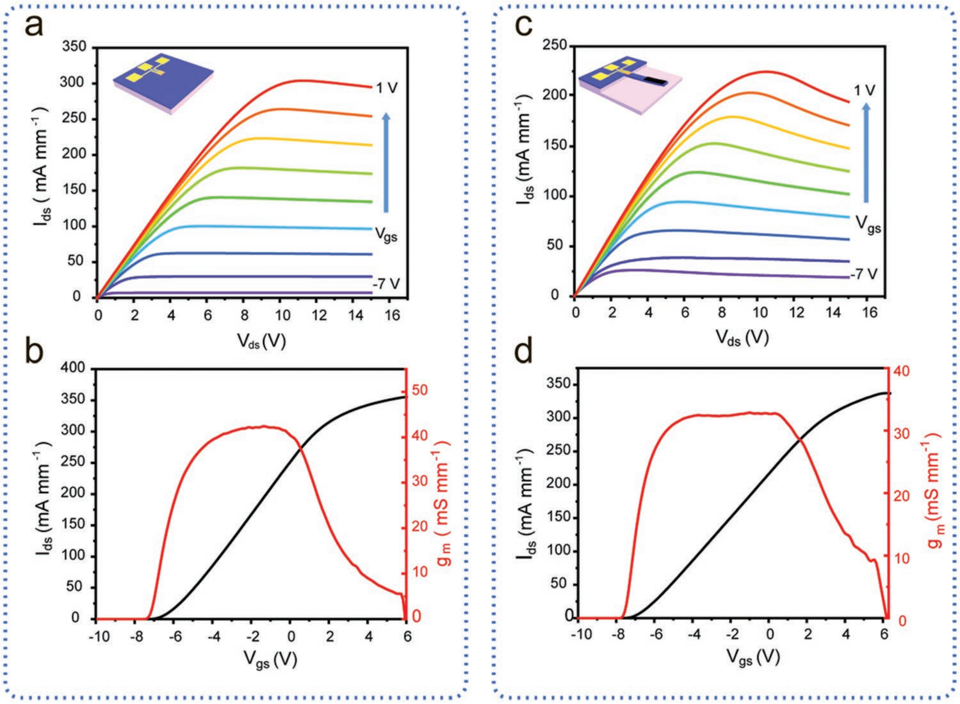

Figure 3. Electrical characteristics of the HEMT (before the fabrication of the cantilever structure) and the as-fabricated MPD. Output ($I_{ds} - V_{ds}$) characteristics of the a) HEMT and c) MPD as the V_{gs} ranging from −7 V to 1 V at a step of 1 V. Transfer ($I_{ds} - V_{gs}$) characteristics of the b) HEMT and (d) MPD measured at $V_{ds} = 10$ V.

illustrates the output characteristics of MPD under various external magnetic fields when $V_{gs} = -5$ V. As the magnetic field increases, the output current density of the MPD increases in both the linear and saturation regions. At $V_{gs} = -5$ V and $V_{ds} = 15$ V, when the magnetic field increases from 0 to 400 mT, the saturation current of the MPD increases from 40.90 to 42.94 mA mm^{-1}. This shows that the output current of MPD can be effectively adjusted by the magnetic field. Moreover, the saturation output current of MPD under the 0–400 mT magnetic field at $V_{ds} = 15$ V in Figure 4c is selected, and the fitting curve is also obtained, as shown in Figure 4d. It is clearly shown that the saturation output current of the MPD has a quasi-linear relationship with the external magnetic field, indicating that the MPD has excellent magnetic field-current modulation performance.

Figure 4e illustrates the output power at $V_{gs} = -5$ V and $V_{ds} = 15$ V under the modulation of magnetic field from 0 to 400 mT. It is clearly shown that the output power density (P) of MPD increases from 18.04 to 18.94 W mm^{-2}, and the changes in output power density (ΔP) increase quasi-linearly with the increase of the external magnetic field. Furthermore, the magnetic field-power modulation characteristics under different gate voltages are systematically measured, as shown in Figure 4f. The output power density shows an increase with the external magnetic field, as a result of the increase of 2DEG concentrations caused by piezotronic effect. Upon the magnetic field of 200 mT, the maximum output power density of the MPD increases up to 25.1, 30.5, 45.1, 53.6, 65.3, 77.0, 85.8 W mm^{-2}, respectively, in response to the V_{gs} various from −5 V to 1 V. It means that the V_{gs} can significantly change the sensitivity of the output power to the external magnetic field. Let us consider a scenario where the MPD acts as a magnetic sensor and actuator on a robot. This means that the driving load of the MPD varies according to different working environments, it may be an LED, a miniature RF signal generator, or a miniature motor. In this case, we can adjust the gate voltage of the MPD to drive the load of the corresponding power level, so that the brightness of the LED, the signal strength of the signal generator and the speed of the motor have corresponding modulation characteristics under different magnetic fields. We have achieved different levels of modulation characteristics of external stress on device output power under different gate voltages in our previous work. The related research results were published in Nat Commun 11, 326 (2020). On this basis, the present work introduces the magnetic field sensing characteristics through the magnetic cantilever structure, which has essentially similar working characteristics. Therefore, it can be concluded that MPD has an ultra-high-output power density, and it can drive external execution devices of different power levels according to the gate voltage after detecting the change of magnetic field, which can be applied as interactive electronics that integrate sensing and execution functions.

2.2. Working Mechanism of MPD

Due to the noncentrosymmetric crystal structure of wurtzite group III-nitride materials, there are spontaneous polarization charges on the surface of the material. Meanwhile, the lattice mismatch between AlGaN, AlN, and GaN films also induces

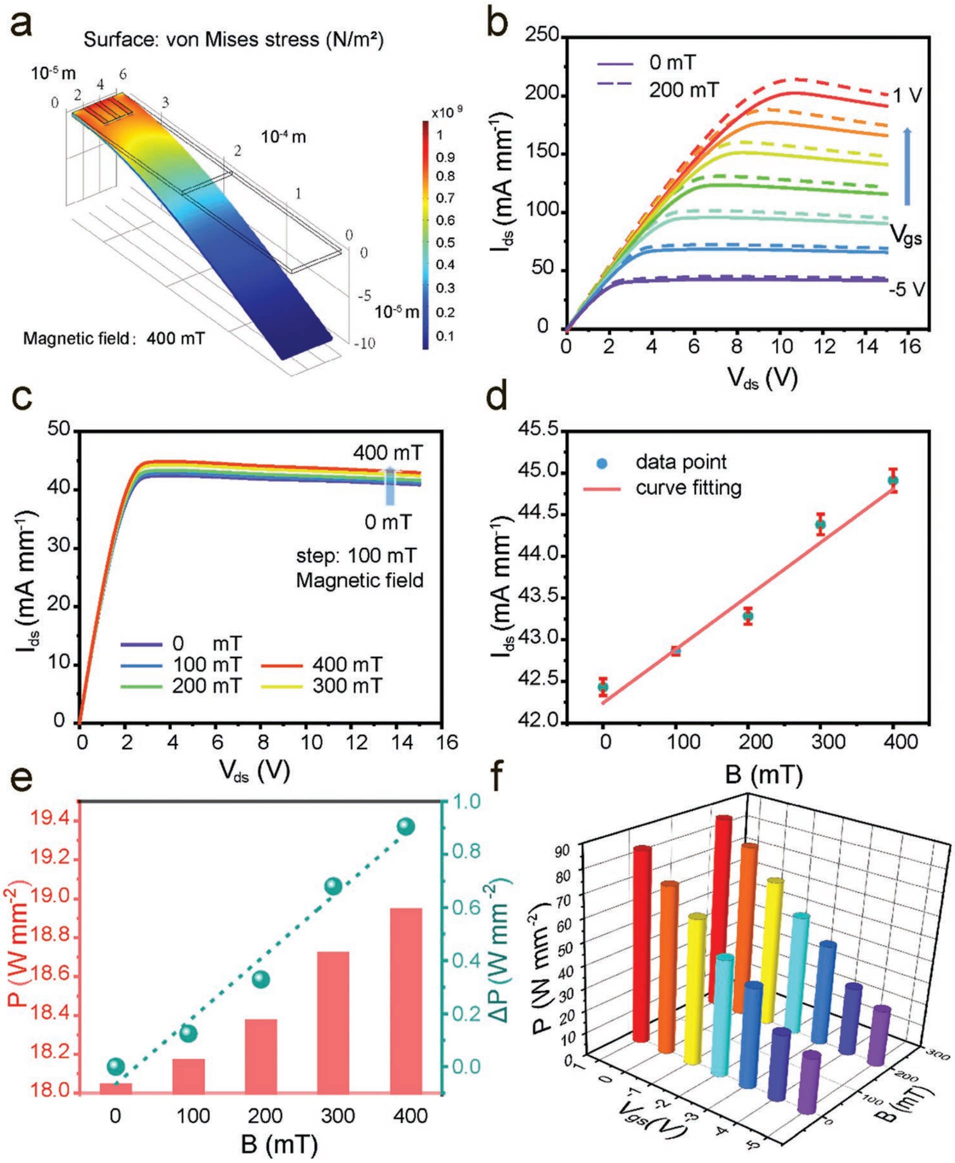

Figure 4. The magnetic field-power modulation characteristics of the MPD. a) The strain distribution of the MPD under an external magnetic field of 400 mT, which is simulated by COMSOL Multiphysics and the magnetic force on the MPD cantilever bends the cantilever down perpendicular to the device surface. b) Output characteristics of the MPD under an external magnetic field of 200 mT, with the gate voltage V_{gs} ranging from −5 V to 1 V at a step of 1 V. c) Output characteristics of the MPD under an external magnetic field from 0 to 400 mT at $V_{gs} = -5$ V. d) The curve fitting of the saturation output current (I_{ds}) in (c) under various magnetic field (0–400 mT) at $V_{ds} = 15$ V. e) Output power density plots of MPD under external magnetic field from 0 to 400 mT at the gate voltage of −5 V. f) 3D plots illustrating the relationship between the output power density and the external magnetic field or gate voltage.

piezoelectric polarization charges at the interface. Studies have shown that the spontaneous polarization charge and piezoelectric polarization charge at the interface jointly modulate the energy band and electrical properties of the AlGaN/AlN/GaN heterojunction.[20,46] Based on the principle of piezotronic effect, when an external strain is applied to the HEMT device along the *c*-axis, the piezoelectric polarization charges at the interface are significantly regulated, thereby adjusting the energy band profile and 2DEG concentration of the AlGaN/AlN/GaN heterojunction, and finally modulating the electrical properties of the HEMT devices.[33] Since a magnetic film is deposited on the front half of the cantilever of the MPD, the external magnetic field can generate a magnetic force at the front end of the cantilever, thereby inducing piezoelectric polarization charges and modulating the output current of the MPD. The external magnetic force is loaded on the front half of the cantilever by using an electric solenoid with an iron core, which can generate a magnetic field along the *c*-axis direction. The loaded magnetic force can be calculated using the Equation (2b). As the magnetic field increases from 0 to 400 mT, the normal force on the cantilever increases from 0 to 0.67 mN. Resulting from the magnetic force introduced by the external magnetic field on the

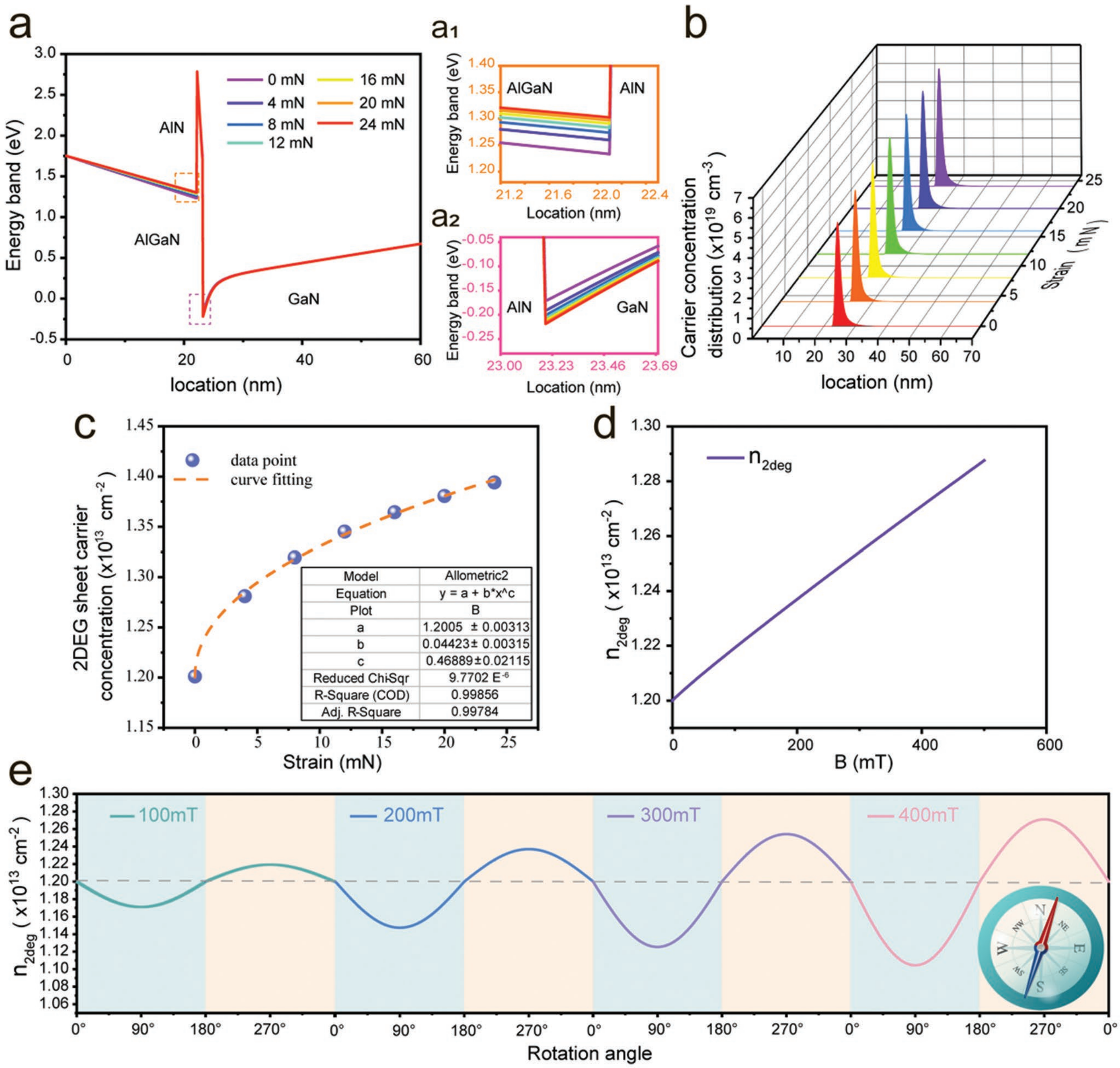

Model	Allometric2
Equation	y = a + b*x^c
Plot	B
a	1.2005 ± 0.00313
b	0.04423± 0.00315
c	0.46889±0.02115
Reduced ChiSqr	9.7702 E-6
R-Square (COD)	0.99856
Adj. R-Square	0.99784

Figure 5. The calculated energy band and 2DEG concentration of AlGaN/AlN/GaN heterojunction. a) The conduction band (E_c) under strain along the *c*-axis of the AlGaN/AlN/GaN heterojunction. The enlarged E_c at (a1) AlGaN/AlN and (a2) AlN/GaN heterojunction labeled by orange rectangular box and pink rectangular box in (a), respectively. b) The carrier concentration distribution in AlGaN/AlN/GaN heterojunction under external strains. c) The 2DEG sheet carrier concentration under external strains, as well as the fitting curve. d) The 2DEG sheet carrier concentration under external magnetic fields, which shows a linear relationship with the magnitude of the magnetic field. e) The 2DEG sheet carrier concentration at different rotation angles under 0–400mT magnetic fields, which shows a sinusoidal relationship with the angle of the magnetic field.

magnetic film, the output current and power of the MPD can be effectively modulated in real time through external magnetic field stimulation.

In order to rationalize our experimental results and reveal the in-depth modulation mechanism of the piezotronic effect on the output characteristics of the MPD, a self-consistent numerical calculation model based on the Schrödinger, Poisson, and Piezoelectric Constitutive equations has been fully developed to simulate the modulation of energy band profile and 2DEG concentration when the magnetic force on the MPD cantilever bends the cantilever down perpendicular to the device surface,[47,48] as shown in **Figure 5**a,b,c,d. Figure 5a presents the calculated conduction band (E_c) of AlGaN/AlN/GaN heterojunction, and the enlarged E_c of the AlGaN/AlN and AlN/GaN heterojunction are shown in Figure 5a1,a2, respectively. As the compressive strain on the cantilever increases (from 0 to 24 mN), the E_c of AlGaN is lifted upward while the E_c of GaN is lowered down, which deepens the potential well of AlN/GaN heterojunction.

Therefore, the carrier concentration distribution of the heterojunction is significantly modulated, as shown in Figure 5b. It is clearly shown that the peak value of carrier concentration increases with strain, indicating that more electrons are confined in the AlN/GaN potential well. According to the theory of semiconductor physics, the 2DEG sheet carrier concentration under different strains can be obtained by integrating the carrier concentration distribution along the *c*-axis, resulting in Table S2 (Supporting Information) and Figure 5c. It illustrates that the 2DEG sheet carrier concentration increases rapidly with external strains (over a range of 0–24 mN).

To further explain the quasi-linear modulation relationship of external magnetic field (B) to source-drain current (I_{ds}) and changes of output power density (ΔP), we perform a curve-fitting on the calculated 2DEG sheet carrier concentration in Figure 5c. The fitting result (Table S3, Supporting Information) shows that the 2DEG concentration is ≈0.5 power of external strain in our strain range and can be expressed as:

$$n_{2deg} = 1.2 + 0.04 * F^{0.47} \tag{2a}$$

where F is the magnetic force, the unit is mN, n_{2deg} is the 2DEG concentration, the unit is $\times\ 10^{13}\ \text{cm}^{-2}$. What needs to be explained here is that in the field of GaN piezoelectric electronics research, strain is usually used to describe the force on the semiconductor device/lattice, which in this paper is exactly the magnetic force on the cantilever. Therefore, both of them are represented by the same Symbol F. Furthermore, based on the magnetic force formula obtained from Maxwell's equation, the strain displays a square relationship with the magnetic field.

$$F = \frac{B^2 A}{2\mu_0} = 4.2 * B^2 \tag{2b}$$

where μ_0 is the vacuum permeability, B is the external magnetic field, the unit is T, A is the area of magnetic film, and the unit is m^2. Hence, combing these two equations, we have eventually derived the linear relationship between 2DEG concentration ($n_{2\text{deg}}$) and external magnetic field (B).

$$n_{2\text{deg}} = 1.2 + 0.168 * B^{0.94} \tag{2c}$$

The curve of the Equation (2c) is shown in Figure 5d. It clearly shows that when the magnetic field increases from 0 to 400 mT, the 2DEG concentration increases quasi-linearly with the external magnetic field. According to semiconductor theory, the source-drain current of AlGaN/GaN HEMT is proportional to the 2DEG concentration. Therefore, we can conclude that the source-drain current and output power are quasi-linearly related to the external magnetic field. The theoretical model agrees well with the experimental result.

The 2DEG sheet carrier concentration when the MPD rotates at different angles under 0–400 mT magnetic fields have also been further simulated to mimic the way birds orient themselves by sensing the angle and magnitude of the geomagnetic field. In the initial state, the cantilever of the MPD is parallel to the magnetic field lines. At this time, the magnetic force perpendicular to the cantilever direction is zero, and the output power is the initial value without the action of the magnetic field. Then the MPD begins to rotate, the cantilever begins to be subjected to a magnetic force that bends upwards perpendicular to the surface of the device, and the output power begins to decrease to varying degrees with the rotation angle. The MPD rotates until the cantilever is parallel to the magnetic field lines again, at which time the magnetic force perpendicular to the cantilever direction becomes zero again and the output power returns to the initial value. After that, the MPD continues to rotate, the cantilever begins to be subjected to a downward magnetic force perpendicular to the surface of the device, and the output power begins to increase to varying degrees with different rotation angles. Finally, the MPD rotates back to the initial state, and the output power also returned to the initial value again. In order to reveal the operating mechanism of the MPD rotating under the magnetic force of different directions, the energy band and 2DEG concentrations under the magnetic force that bends the cantilever up perpendicular to the device surface were calculated, detailed in Supplementary Note S1. The results show that the 2DEG concentration of MPD exhibits a linear decreasing relationship with the external magnetic force. Combining these two calculation results and taking into account the angle of rotation, the relationship between the 2DEG concentration of MPD and the rotation angle was calculated

$$n_{2\text{deg}} = 1.2 + 0.168 * B^{0.94} * \cos\left(\frac{\theta\pi}{180}\right) \tag{2d}$$

$$n_{2\text{deg}} = 1.2 - 0.21 * B^{0.86} * \cos\left(\frac{(\theta - 180)\pi}{180}\right) \tag{2e}$$

where the θ is the rotation angle and the curve is shown in Figure 5e. It clearly illustrates that the 2DEG concentration of MPD has an approximately sinusoidal relationship with the rotation angle, and its maximum value increases significantly with the increase of the magnetic field. It is worth noting that the 2DEG modulation curve of MPD during the rotation process is not symmetrical, that is, the power output curve is not symmetrical in the case of rotation. This phenomenon is obtained based on computational simulation and mathematical analysis. We mentioned above that the modulation properties of the 2DEG concentration by the external magnetic field are based on the piezoelectric effect. The essence of this effect is that the external stress causes lattice deformation, which changes the piezoelectric polarization charge on the surface of the material and in turn affects the energy band distribution and carrier concentration. During the rotation process, the upward and downward forces on the MPD cantilever perpendicular to the device surface result in different lattice deformations in the surface active region, and this difference is finally reflected on the 2DEG curve. Therefore, it can be concluded that the output current and power of MPD show a sinusoidal relationship with the angle of the magnetic field, and a linear relationship with the magnitude of the magnetic field when sensing different external magnetic fields. This indicates that the output current and power of MPD can be effectively modulated by the angle and magnitude of the magnetic field, showing excellent orientation and sensing capabilities.

3. Conclusion

In summary, we demonstrate a magnetosensory power device that can utilize external magnetic field to modulate the output power of the device by the emulation of magnetoreception in nature. Based on the piezotronic effect, the strain-induced piezoelectric polarization charges can modify the energy band profile of the local AlGaN/AlN/GaN heterojunction, and effectively adjust the 2DEG concentration to tune/control the output power of the MPD. Due to the design of the magnetic cantilever of the MPD, the external magnetic field can introduce a normal compressive strain at the front end of the cantilever, thereby triggering piezotronic effect. Under the action of the external magnetic field of 0–400 mT, when the gate voltage is −5 V, the saturation output power density of MPD increases quasi-linearly from 18.04 to 18.94 W mm^{-2}, showing good magnetic field-power modulation characteristics. Meanwhile, the gate voltage of MPD can control the working point of the output power in a larger range. The maximum output power density of MPD can reach 85.8 W mm^{-2} at 1 V gate voltage under 200 mT magnetic field, thereby realizing the two-dimensional control of the output power by the external magnetic field and the gate voltage. This work not only provides insights into interactive electronics that integrate sensing and control functionalities, but also promotes the development of bionic AI smart devices.

4. Experimental Section

Device Fabrication: The MPD was fabricated with III-Nitride epitaxial layers by metal-organic chemical vapor deposition (MOCVD) on Si substrate (111). The epitaxial layer structure consists of AlGaN (30 nm, 30% Al)/AlN (1 nm)/GaN (4.3 µm)/AlGaN buffer layer/Si substrate. The mesa was etched using an inductively coupled plasma etching system (ICP, SENTECH SI 500) etch process based on $BCl_3/Cl_2/Ar$. In order to form the ohmic contact and Schottky contact, Ti/Al/Ni/Au (20 nm/120 nm/45 nm/55 nm) metal stack deposition was evaporated using an electron beam evaporation system (Denton Vacuum Explore 14) and annealed at 900 °C in N_2 environment for 30 s using a rapid thermal processing system (LABSYS RTP-1200), and Ni/Au (80 nm/50 nm) was evaporated for gate metallization respectively. Then the magnetic film $(Fe_{90}Co_{10})_{78}Si_{12}B_{10}$ (500 nm) was deposited by magnetron sputtering (Denton Discovery 635). Finally, the ICP-based dry etching was performed by combing the anisotropic/isotropic etching to fabricate the cantilever using an inductively coupled plasma etching system (ICP, SENTECH SI 500) etch process based on $BCl_3/Cl_2/Ar$ and $SF_6/O_2/Ar$. The main steps of the etching process of the cantilever structure based on ICP dry etching are as follows: Step 1: anisotropic etching of GaN. The photoresist patterned GaN thin film (thickness: 5 µm) was completely etched with the anisotropic etching recipe ($BCl_3/Cl_2/Ar$: 10/32/5 sccm; Power: 550 W; Process time: 30 min). Step 2: isotropic etching of Si. The cantilever structure was fabricated with the isotropic etching recipe ($SF_6/O_2/Ar$: 30/5/10 sccm; Power: 800 W; Process time: 25 min). The manufactured cantilever had dimensions of $350 \times 60 \times 5$ μm^3, with the embedded HEMT had a mesa dimension of 34×34 μm^2 and a gate length of 5 µm.

Material, Electrical and Magnetic Characterizations: The morphology of the MPD was observed by using field-emission scanning electron microscopy (Nova Nano SEM 450) operated at 10 kV. The Raman measurements with 532 nm laser before and after dry etching were performed with a micro-Raman spectrometer (LabRAM HR Evolution) at room temperature. External Magnetic field along *c*-axis was applied on cantilevers through the electric solenoid with an iron core designed of our own design. By changing the input current of electric solenoid, a compressive magnetic force was loaded on the cantilevers. Keysight B1500A was used to measure the electrical characteristics of the MPD under various magnetic fields.

Supporting Information

Supporting Information is available from the Wiley Online Library or from the author.

Acknowledgements

X.Z., Q.H., and W.S. contributed equally to this work. The authors thank for the support from the National Natural Science Foundation of China (52192610, 52173298, and 61904012), and the National Key R & D Project from the Minister of Science and Technology (2021YFA1201603), Supported by the Fundamental Research Funds for the Central Universities.

Conflict of Interest

The authors declare no conflict of interest.

Data Availability Statement

The data that support the findings of this study are available from the corresponding author upon reasonable request.

Keywords

AlGaN/GaN HEMT, cantilever structure, interactive electronics, magnetoreception, power device

Received: August 25, 2022
Revised: November 27, 2022

[1] D. Dreyer, B. Frost, H. Mouritsen, A. Gunther, K. Green, M. Whitehouse, S. Johnsen, S. Heinze, E. Warrant, *Curr. Biol.* **2018**, *28*, 2160.
[2] J. H. Fischer, M. J. Freake, S. C. Borland, J. B. Phillips, *Anim. Behav.* **2001**, *62*, 1.
[3] F. J. Diego-Rasilla, V. Perez-Mellado, A. Perez-Cembranos, *Naturwissenschaften* **2017**, *104*, 13.
[4] L. C. Naisbett-Jones, N. F. Putman, M. M. Scanlan, D. L. G. Noakes, K. J. Lohmann, *J. Exp. Biol.* **2020**, *223*.
[5] K.-P. Ossenkopp, R. Barbeito, *Neurosci. Biobehav. Rev.* **1978**, *2*, 255.
[6] T. Ritz, S. Adem, K. Schulten, *Biophys. J.* **2000**, *78*, 707.
[7] D. Kishkinev, N. Chernetsov, A. Pakhomov, D. Heyers, H. Mouritsen, *Curr. Biol.* **2015**, *25*, R822.
[8] H. Mouritsen, T. Ritz, *Curr. Opin. Neurobiol.* **2005**, *15*, 406.
[9] J. M. Ong, L. da Cruz, *Clin. Exp. Ophthalm.* **2012**, *40*, 6.
[10] L. Q. Zhu, C. J. Wan, L. Q. Guo, Y. Shi, Q. Wan, *Nat. Commun.* **2014**, *5*, 1.
[11] X. Liao, W. Song, X. Zhang, C. Yan, T. Li, H. Ren, C. Liu, Y. Wang, Y. Zheng, *Nat. Commun.* **2020**, *11*, 1.
[12] Y. Cao, Y. J. Tan, S. Li, W. W. Lee, H. Guo, Y. Cai, C. Wang, B. C.-K. Tee, *Nat. Electron.* **2019**, *2*, 75.

[13] G. S. C. Bermúdez, H. Fuchs, L. Bischoff, J. Fassbender, D. Makarov, *Nat. Electron*. **2018**, *1*, 589.
[14] P. Makushko, O. Mata, S. E. , C. Bermúdez, S. G. , M. Hassan, S. Laureti, C. Rinaldi, F. Fagiani, G. Barucca, N. Schmidt, Y. Zabila, *Adv. Funct. Mater.* **2021**, 2101089.
[15] G. S. C. Bermúdez, D. D. Karnaushenko, D. Karnaushenko, A. Lebanov, L. Bischoff, M. Kaltenbrunner, J. Fassbender, O. G. Schmidt, D. Makarov, *Sci. Adv.* **2018**, *4*, eaao2623.
[16] M. Melzer, J. I. Mönch, D. Makarov, Y. Zabila, G. S. Cañón Bermúdez, D. Karnaushenko, S. Baunack, F. Bahr, C. Yan, M. Kaltenbrunner, *Adv. Mater.* **2015**, *27*, 1274.
[17] C. Bermúdez, G. S. , D. Makarov, *Adv. Funct. Mater.* **2021**, *31*, 2007788.
[18] N. Münzenrieder, D. Karnaushenko, L. Petti, G. Cantarella, C. Vogt, L. Büthe, D. D. Karnaushenko, O. G. Schmidt, D. Makarov, G. Tröster, *Adv. Electron. Mater.* **2016**, *2*, 1600188.
[19] T. Ueda, *Jpn. J. Appl. Phys.* **2019**, *58*, SC0804.
[20] O. Ambacher, B. Foutz, J. Smart, J. Shealy, N. Weimann, K. Chu, M. Murphy, A. Sierakowski, W. Schaff, L. Eastman, *J. Appl. Phys.* **2000**, *87*, 334.
[21] D. Jena, J. Simon, Y. Cao, K. Goodman, J. Verma, S. Ganguly, G. Li, K. Karda, V. Protasenko, C. Lian, *ArXiv* **2010**.
[22] E. Yu, X. Dang, P. Asbeck, S. Lau, G. Sullivan, *Meas. Phenom*. **1999**, *17*, 1742.
[23] C. Pan, J. Zhai, Z. L. Wang, *Chem. Rev.* **2019**, *119*, 9303.
[24] Z. L. Wang, W. Wu, C. Falconi, *MRS Bull.* **2018**, *43*, 922.
[25] W. Sha, J. Zhang, S. Tan, X. Luo, W. Hu, *J. Phys. D: Appl. Phys.* **2019**, *52*, 213003.
[26] X. Wang, R. Yu, C. Jiang, W. Hu, W. Wu, Y. Ding, W. Peng, S. Li, Z. L. Wang, *Adv. Mater.* **2016**, *28*, 7234.
[27] Z. L. Wang, J. Song, *Science* **2006**, *312*, 242.
[28] X. Huang, C. Du, Y. Zhou, C. Jiang, X. Pu, W. Liu, W. Hu, H. Chen, Z. L. Wang, *ACS Nano* **2016**, *10*, 5145.
[29] T. Liu, D. Li, H. Hu, X. Huang, Z. Zhao, W. Sha, C. Jiang, C. Du, M. Liu, X. Pu, B. Ma, W. Hu, Z. L. Wang, *Nano Energy* **2020**, *67*, 104218.
[30] Q. Guo, D. Li, Q. Hua, K. Ji, W. Sun, W. Hu, Z. L. Wang, *Nano Lett.* **2021**, *21*, 4062.
[31] T. Liu, C. Jiang, X. Huang, C. Du, Z. Zhao, L. Jing, X. Li, S. Han, J. Sun, X. Pu, J. Zhai, W. Hu, *Nano Energy* **2017**, *39*, 53.
[32] C. Jiang, T. Liu, C. Du, X. Huang, M. Liu, Z. Zhao, L. Li, X. Pu, J. Zhai, W. Hu, Z. Lin Wang, *Nanotechnology* **2017**, *28*, 455203.
[33] J. Zhu, X. Zhou, L. Jing, Q. Hua, W. Hu, Z. L. Wang, *ACS Nano* **2019**, *13*, 13161.
[34] S. Zhang, B. Ma, X. Zhou, Q. Hua, J. Gong, T. Liu, X. Cui, J. Zhu, W. Guo, L. Jing, W. Hu, Z. L. Wang, *Nat. Commun.* **2020**, *11*, 326.
[35] W. Sha, Q. Hua, Y. Shi, J. Wang, X. Cui, Z. Dong, B. Wang, J. Niu, W. Hu, *J. Mater. Chem. C* **2022**, *10*, 11783.
[36] S. Johnsen, K. J. Lohmann, *Nat. Rev. Neurosci.* **2005**, *6*, 703.
[37] M. Frommberger, J. McCord, E. Quandt, *IEEE Trans. Magn.* **2004**, *40*, 2703.
[38] C. Müller, P. Durdaut, R. B. Holländer, A. Kittmann, V. Schell, D. Meyners, M. Höft, E. Quandt, J. McCord, *Adv. Electron. Mater.* **2022**, 2200033.
[39] L. Thormählen, D. Seidler, V. Schell, F. Munnik, J. McCord, D. Meyners, *Sensors* **2021**, *21*, 8386.
[40] B. Tong, X. Yang, J. Ouyang, G. Lin, Y. Zhang, S. Chen, *J. Appl. Phys.* **2014**, *115*, 17D904.
[41] M. Yang, Z. Lin, J. Zhao, Y. Wang, Z. Li, Y. Lv, Z. Feng, *Superlattices Microstruct.* **2015**, *85*, 43.
[42] S. Choi, E. Heller, D. Dorsey, R. Vetury, S. Graham, *J. Appl. Phys.* **2013**, *113*, 093510.
[43] J. Ladroue, A. Meritan, M. Boufnichel, P. Lefaucheux, P. Ranson, R. Dussart, *J. Vac. Sci. Technol., A* **2010**, *28*, 1226.
[44] S. Pearton, R. Shul, F. Ren, *M R S Internet J. Nitride Semicond. Res.* **2000**, *5*, e11.
[45] K. C. Huang, W. H. Lan, K. F. Huang, *Jpn. J. Appl. Phys.* **2004**, *43*, 82.
[46] A. E. Romanov, T. J. Baker, S. Nakamura, J. S. Speck, *J. Appl. Phys.* **2006**, *100*, 023522.
[47] B. Jogai, *J. Appl. Phys.* **2002**, *91*, 3721.
[48] I. H. Tan, G. Snider, L. Chang, E. Hu, *J. Appl. Phys.* **1990**, *68*, 4071.